Highlights

Onset-centered complexity signatures of GOES flare class in Konus-WIND G1–G3 time series

D. Sierra-Porta, J. D. Pérez-Navarro, J. D. Petro-Ramos

- Konus-WIND G1 ($\sim$20–80 keV): monotonic C$\rightarrow$M$\rightarrow$X scaling in fractal dimension, permutation entropy, and statistical complexity.
- Konus-WIND G2 ($\sim$80–300 keV): strongest class discrimination via LZ complexity and Hjorth complexity, including a sign reversal for X-class events.
- Konus-WIND G3 ($\sim$300–1200 keV): onset-related shifts present but class discrimination weaker, concentrated in C vs. X contrasts.

Onset-centered complexity signatures of GOES flare class in Konus-WIND G1–G3 time series

D. Sierra-Porta[a,*], J. D. Pérez-Navarro[b] and J. D. Petro-Ramos[b]

[a] *Universidad Tecnológica de Bolívar. Grupo de Investigación Gravitación y Matemática Aplicada - GIGMA & Grupo de Investigación Física Aplicada y Procesamiento de Imágenes y Señales - FAPIS. , Parque Industrial y Tecnológico Carlos Vélez Pombo Km 1 Vía Turbaco., Cartagena de Indias, 130010, Bolívar, Colombia*

[b] *Universidad Tecnológica de Bolívar. Escuela de Transformación Digital. , Parque Industrial y Tecnológico Carlos Vélez Pombo Km 1 Vía Turbaco., Cartagena de Indias, 130010, Bolívar, Colombia*

ARTICLE INFO

Keywords:
Solar flares
Konus-WIND
GOES classification
permutation entropy
statistical complexity
Higuchi fractal dimension
Hjorth parameters
nonparametric tests
false discovery rate

ABSTRACT

The high-energy emission from solar flares demonstrates highly variable and often complex light curves, whose temporal structure may contain information beyond standard amplitude-based summaries. Using the Konus-WIND solar flare observations, we carried out an investigation into the statistical association between the onset-centered changes in geometric and complexity-based descriptors and GOES flare classes. Our study was based on the data from the background-subtracted count rates from the event catalogue in three energy channels: G1 (20–80 keV), G2 (80–300 keV) and G3 (300–1200 keV). The observation of each event was segmented into pre-onset ("before") and post-onset ("after") intervals defined by bin boundaries relative to the trigger time. For each channel and segment we computed five descriptors: Higuchi fractal dimension, normalized permutation entropy, statistical complexity C_{JS} in the complexity–entropy framework, normalized Lempel–Ziv complexity (median-binarized), and Hjorth complexity. We summarized onset-associated changes by paired differences $\Delta = after - before$ and assessed class dependence using nonparametric hypothesis tests with Benjamini–Hochberg false-discovery-rate control.

In different channels, most descriptors showed non-zero onset-associated shifts, and the magnitude of Δ was significantly different for most channel–descriptor combinations across GOES classes. The strongest monotonic class scaling was observed in the G1 channel for Higuchi fractal dimension, permutation entropy, and C_{JS}, while the clearest separation in the G2 channel was provided by normalized Lempel–Ziv and Hjorth complexity, including a marked Hjorth-complexity transition for X-class events. In the G3 channel, onset-related changes remained evident but between-class discrimination was weaker overall, with Higuchi fractal dimension showing near class-invariant Δ. The obtained results provide conservative population-level evidence that multi-channel onset-centered complexity and geometric descriptors are statistically related to flare class, and motivate future work on integrating additional physical covariates and strictly validated classification models.

1. Introduction

Solar flares are rapid releases of magnetic energy in the solar atmosphere that produce broadband electromagnetic emission and are frequently accompanied by particle acceleration and complex, bursty light-curve morphologies (Fletcher, Dennis, Hudson, Krucker, Phillips, Veronig, Battaglia, Bone, Caspi, Chen et al., 2011; Benz, 2017; Cliver, Schrijver, Shibata and Usoskin, 2022). Beyond integrated quantities such as peak flux, duration, and fluence, flare time series often exhibit intermittent variability across multiple time scales, a behaviour rooted in the self-organised critical dynamics of the magnetised corona (Lu and Hamilton, 1991; Aschwanden, Crosby, Dimitropoulou, Georgoulis, Hergarten, McAteer, Milovanov, Mineshige, Morales, Nishizuka et al., 2016). This suggests that the temporal organisation of the emission may encode additional information about the underlying energy-release and acceleration processes (Holman, Aschwanden, Aurass, Battaglia, Grigis, Kontar, Liu, Saint-Hilaire and Zharkova, 2011; Schrijver, 2009). Quantifying such organisation in a way that is robust across instruments and event populations remains an active challenge in solar and heliospheric physics.

*Corresponding author: D. Sierra-Porta (dporta@utb.edu.co)

dporta@utb.edu.co (D. Sierra-Porta); perezjuan@utb.edu.co (J.D. Pérez-Navarro); jpetro@utb.edu.co (J.D. Petro-Ramos)

ORCID(s): 0000-0003-3461-1347 (D. Sierra-Porta); 0009-0008-5689-314X (J.D. Pérez-Navarro); 0009-0009-2407-2694 (J.D. Petro-Ramos)

From a physical standpoint, the temporal structure of high-energy flare emission is closely linked to the impulsive-phase processes of magnetic reconnection, rapid energy conversion, and particle acceleration in the corona and lower atmosphere. In the standard flare scenario, reconnection restructures coronal magnetic fields, releases stored magnetic free energy, and produces accelerated electron populations that precipitate along field lines and deposit energy in dense chromospheric targets. This "thick-target" interaction yields hard X-ray bremsstrahlung with strongly time-variable light curves that often consist of clustered spikes and bursts, reflecting the intermittent and fragmented nature of the energy-release and acceleration region (Holman et al., 2011; Fletcher et al., 2011; Benz, 2017). At the same time, flare emission evolves spectrally and temporally through a combination of thermal plasma heating, nonthermal particle production, and transport effects, so that the same GOES class can correspond to markedly different high-energy morphologies and degrees of burstiness (Dennis, 1985).

These considerations motivate analysing flare signals in a channel-resolved manner. Broad energy channels, such as those provided by Konus-WIND, sample different mixtures of thermal and nonthermal contributions and can emphasise different stages or components of the impulsive evolution (Lysenko, Ulanov, Kuznetsov, Fleishman, Frederiks, Kashapova, Sokolova, Svinkin and Tsvetkova, 2022). Consequently, channel-dependent changes in multi-scale roughness, ordinal pattern diversity, and symbolic/algorithmic complexity are not unexpected *a priori*, but they require systematic population-level evaluation to establish whether they are statistically detectable and reproducible across event classes. Here we adopt a conservative strategy: we quantify onset-associated changes via paired pre/post differences and assess class dependence using nonparametric hypothesis testing with explicit multiple-testing control, interpreting the resulting trends as statistical signatures of temporal reorganisation rather than as direct measurements of specific microphysical mechanisms (Bandt and Pompe, 2002; Rosso, Larrondo, Martin, Plastino and Fuentes, 2007).

In operational and statistical studies, flare magnitude is commonly summarised using the GOES soft X-ray (SXR) classification (B, C, M, X), defined by the peak SXR flux in the 1–8 Å band (Veronig, Temmer, Hanslmeier, Otruba and Messerotti, 2002; Cliver et al., 2022). While GOES class provides a widely used reference scale, it is fundamentally a thermal proxy and does not uniquely determine the structure of higher-energy emission. High-energy channels, which are more sensitive to nonthermal components and impulsive-phase dynamics, can display large event-to-event variability even within the same GOES class (Dennis, 1985; Holman et al., 2011). This motivates complementary, time-series-based approaches that characterise flare signals not only by amplitude but also by their temporal geometry and complexity (Morikawa and Nakamichi, 2023; Zimovets, McLaughlin, Srivastava, Kolotkov, Kuznetsov, Kupriyanova, Cho, Inglis, Reale, Pascoe et al., 2021).

A broad set of methods has been proposed to describe complexity in physical time series. Multi-scale geometric roughness can be captured by the Higuchi fractal dimension (Higuchi, 1988), a robust estimator of the scaling properties of irregular time series that has been applied across diverse physical systems (Wanliss and Wanliss, 2022; Carrizales-Velázquez, Donner and Guzmán-Vargas, 2021). Ordinal-pattern statistics, particularly permutation entropy (Bandt and Pompe, 2002) and statistical complexity C_{JS} in the complexity–entropy framework (Rosso et al., 2007), characterise local pattern diversity and structured departures from randomness; both descriptors have been used to distinguish dynamical regimes in laboratory and space plasmas (Weck, Schaffner, Brown and Wicks, 2015; Kilpua, Good, Ala-Lahti, Osmane and Koikkalainen, 2024). Algorithmic-complexity surrogates, specifically normalised Lempel–Ziv complexity (Lempel and Ziv, 1976), quantify the compressibility of symbolic representations and have proven sensitive to changes in signal regularity across a wide range of applications (Rosso et al., 2007; Rosso, Carpi, Saco, Ravetti, Plastino and Larrondo, 2012). Finally, Hjorth complexity (Hjorth, 1970) provides a time-domain descriptor sensitive to local waveform structure and effective dynamical bandwidth, complementing frequency-agnostic measures (Morikawa and Nakamichi, 2023).

These descriptors capture different facets of temporal organisation and can be computed directly from observed time series and compared across events in a standardised manner. However, systematic, event-level evaluations of whether these descriptors exhibit statistically detectable differences across flare classes—and whether such differences depend on energy channel—remain relatively limited in solar physics, particularly when adopting conservative nonparametric inference and explicit multiple-testing control (Fletcher, 2024).

In this work, we perform an event-centred, pre/post-onset analysis of Konus-WIND solar-flare time series. Using the KW-Sun event catalogue (Lysenko et al., 2022), we extract background-subtracted count-rate series in three energy channels (G1, G2, and G3) for each event and split each channel into pre-onset and post-onset segments defined relative to the trigger time. For each segment we compute a compact set of geometric and complexity-based descriptors: Higuchi fractal dimension (Higuchi, 1988), normalised permutation entropy (Bandt and Pompe, 2002), statistical complexity

C_{JS} in the complexity–entropy framework (Rosso et al., 2007), normalised Lempel–Ziv complexity (Lempel and Ziv, 1976), and Hjorth complexity (Hjorth, 1970).

Our goal is deliberately modest and primarily statistical. Specifically, we address the following research question: *Do onset-centered changes in geometric and complexity-based descriptors of Konus-WIND count-rate time series differ systematically across GOES flare classes (C, M, X), and does this class dependence vary across energy channels?* To answer this question, we compute paired pre/post-onset differences $\Delta = after - before$ for each event and channel, and test whether the resulting Δ distributions differ across classes using nonparametric hypothesis tests with Benjamini–Hochberg false-discovery-rate correction (Benjamini and Hochberg, 1995). By focusing on paired differences, robust summaries (median and IQR), and conservative nonparametric inference, we aim to provide a reproducible population-level baseline for describing flare time-series organisation.

2. Materials and Methods

2.1. Data

We used the Konus-WIND solar-flare event list provided by the Ioffe Institute (KW-Sun project), downloaded as a comma-separated catalogue file (`KonusWIND_SolarFlares.txt`: `http://www.ioffe.ru/LEA/kwsun/KW_spectrum_times.txt`). For each triggered event, the catalogue reports the trigger date and time, the associated GOES soft X-ray class (B, C, M, X), auxiliary GOES timing fields (begin/max/end), and a direct URL to the corresponding Konus-WIND light-curve file. In our workflow, the event catalogue was stored locally as `KW_All_Events.csv`.

Each event URL points to an ASCII light-curve file named `KWYYYYMMDD_TSSSSS.txt` (`http://www.ioffe.ru/LEA/kwsun/data/`). These files provide binned count-rate series in three Konus-WIND energy channels (G1, G2, G3) together with background-subtracted versions of each channel. Following the KW-Sun convention, the three channels correspond approximately to ∼20–80 keV (G1), ∼80–300 keV (G2), and ∼300–1200 keV (G3), with exact boundaries subject to calibration and operational conditions (Lysenko et al., 2022). In this study we analyzed only the background-subtracted series.

The G3 channel (∼300–1200 keV) deserves particular note: emission at these energies probes the most energetic nonthermal electron populations and includes contributions from the 511 keV positron annihilation line in the strongest events. This energy range is directly relevant for the relationship between flare particle acceleration and solar energetic particle (SEP) productivity (Shih, Lin and Smith, 2009; Holman et al., 2011).

Figure 1 shows the annual distribution of C-, M-, and X-class events in the KW-Sun catalogue across the full operational period of Konus-WIND (1994–2025). The dataset spans three solar cycles, with peak event rates during the maxima of SC23 (1999–2001) and SC24 (2011–2014). Gaps in annual coverage (notably 2008–2009 and 2018–2019) coincide with the SC23/SC24 and SC24/SC25 solar minima. In the most recent era (SC25, 2020–2025), M- and X-class events dominate the sample owing to the rising phase of the current cycle, while C-class events are comparatively underrepresented ($n_C = 29$); the implications of this imbalance for the temporal stability analysis are discussed in Section 3.1.

2.2. Data retrieval and preprocessing

From each event file we extracted the background-subtracted channel series `G1bgsub`, `G2bgsub`, and `G3bgsub`. Non-numeric values were coerced to missing values and removed prior to descriptor computation. Each event file includes two time columns, t_1 and t_2, representing the start and end of each time bin relative to the trigger time (onset). We defined two non-overlapping segments: (i) a pre-onset segment ("before") and (ii) a post-onset segment ("after"). A bin was assigned to the pre-onset segment if $t_1 < 0$ and $t_2 < 0$, and to the post-onset segment if $t_1 \geq 0$ and $t_2 \geq 0$. Bins crossing onset ($t_1 < 0 \leq t_2$) were excluded from all descriptor calculations to avoid mixing pre- and post-onset behavior within a single bin.

Figure 2 illustrates this segmentation procedure on a representative Konus-WIND flare event. The three background-subtracted channels (G1, G2, G3) are shown as a function of time relative to the trigger ($t = 0$), with pre-onset bins coloured in blue, post-onset bins in red, and the single crossing bin excluded from analysis shown in grey. The figure highlights the diversity of segment lengths and signal amplitudes across channels that is characteristic of the KW-Sun event population.

The Konus-WIND trigger time, used here as the segmentation reference ($t = 0$), is not identical to the GOES soft X-ray begin time. The trigger fires when the background-subtracted count rate in G1 exceeds an instrumental threshold and its rate of change satisfies a prescribed condition — a criterion sensitive to the onset of significant nonthermal hard X-ray emission rather than to the earlier onset of thermal chromospheric heating. Across the 1,174 events in the catalogue, the trigger systematically follows the GOES soft X-ray begin time by a median of 248 s (range: 5.6–9831 s), with the lag increasing with flare class (C: 201 s; M: 267 s; X: 378 s). This ordering is consistent with the known temporal separation between the onset of chromospheric evaporation, which produces the soft X-ray flux detected by GOES, and the onset of the dominant impulsive hard X-ray bremsstrahlung phase (Holman et al., 2011; Dennis, 1985; Neupert, 1968). Accordingly, the pre-trigger ("before") segment captures the thermal precursor and pre-impulsive phase, while the post-trigger ("after") segment captures the impulsive and post-impulsive hard X-ray emission — the physically relevant boundary for characterising temporal organisation in the G1–G3 channels. A robustness analysis stratifying events by trigger lag confirms that the five primary class-dependent descriptors are significant in both groups (Appendix A.4).

Descriptor estimation was performed only when the segment contained at least $n_{\min} = 80$ valid (finite) samples; segment–event combinations failing this requirement were excluded for the corresponding channel and descriptor. This minimum-length criterion serves a dual purpose: it ensures that ordinal-pattern and fractal estimators are computed on samples of sufficient size to be statistically reliable (Bandt and Pompe, 2002; Higuchi, 1988), and it implicitly excludes flare–channel combinations where the background-subtracted signal is too weak or noisy to yield interpretable time-series structure.

Not all Konus-WIND triggered events produce detectable emission across all three energy channels. Hard X-ray emission above 80 keV (G2) and especially above 300 keV (G3) requires substantial nonthermal particle acceleration, and may be absent or marginal in weaker flares (Holman et al., 2011; Dennis, 1985). To assess the impact of low-signal events on the G3 results, we computed an event-level peak signal-to-noise ratio for the G3 channel, defined as

$$\mathrm{SNR}_{G3} = \frac{\max(\mathrm{G3bgsub}_{\mathrm{after}})}{\mathrm{std}(\mathrm{G3bgsub}_{\mathrm{before}})}, \tag{1}$$

where the numerator is the maximum background-subtracted count rate in the post-onset segment and the denominator is the standard deviation of the pre-onset segment, providing a robust estimate of the peak signal amplitude relative to the pre-flare variability level. Of the 1,156 events in the analysis sample, 1,152 (99.7%) yielded $\mathrm{SNR}_{G3} \geq 3.0$, indicating detectable emission above 300 keV. Only 4 events ($< 0.3\%$) fell below this threshold and were treated as having no pronounced G3 signal. The practical impact of this criterion is therefore negligible for the present dataset: a supplementary analysis restricted to events with $\mathrm{SNR}_{G3} \geq 3.0$ ($n = 1{,}139$ after delta-table filtering; see Section A) yields results that are indistinguishable from those obtained on the full G3 sample.

2.3. Geometric and complexity descriptors

For each event, channel, and segment (before/after), we computed five descriptors that together capture complementary and non-redundant aspects of the temporal organisation of hard X-ray count-rate signals. The selection was guided by three criteria: (i) applicability to short, non-stationary segments without distributional assumptions; (ii) coverage of distinct facets of temporal complexity — multi-scale geometric roughness, ordinal pattern diversity, algorithmic compressibility, and local waveform structure; and (iii) established use in physical time-series analysis, including space and laboratory plasmas (Weck et al., 2015; Kilpua et al., 2024; Morikawa and Nakamichi, 2023). The five descriptors span the space of complexity measures from fractal scaling (capturing long-range self-similarity) to information-theoretic quantities (capturing departure from randomness and ordinal pattern diversity) to symbolic complexity (capturing compressibility of binarised sequences) and time-domain waveform structure (capturing effective dynamical bandwidth). Because Konus-WIND channels sample both thermal and nonthermal emission components with markedly different temporal profiles across flare classes, and because segment lengths vary substantially across events, no single descriptor is expected to be universally optimal; the multichannel, multi-descriptor design is therefore deliberate. Specifically, we computed:

- **Higuchi fractal dimension** (D_H), a multi-scale geometric roughness measure of the time series;
- **Normalized permutation entropy** (H_{perm}), computed from ordinal patterns and reported in normalized form;
- **Statistical complexity** (C_{JS}) in the complexity–entropy framework, combining normalized Shannon entropy with a normalized Jensen–Shannon divergence relative to the uniform ordinal distribution;

- **Normalized Lempel–Ziv complexity** (LZ), computed on a binarized version of the segment and reported in normalized form;
- **Hjorth complexity**, a time-domain descriptor sensitive to local waveform structure and effective dynamical bandwidth.

Standardization. Unless otherwise stated, each segment was standardized by a z-score transform before computing descriptors, to reduce scale effects across events and channels.

Ordinal-pattern settings for H_{perm} and C_{JS}. Permutation-based quantities were computed using the Bandt–Pompe ordinal-pattern approach (Bandt and Pompe, 2002; Rosso et al., 2007). We used embedding order $m = 3$ and delay $\tau = 1$; the latter corresponds to consecutive samples and avoids introducing additional assumptions about the characteristic time scale of the signal, which can vary substantially across flare classes and energy channels.

The choice of $m = 3$ as the baseline embedding order was guided by two complementary constraints. First, the minimum-segment criterion: with $n_{\text{min}} = 80$ valid samples and $m = 3$, each segment yields at least $\lfloor N/m! \rfloor \geq 13$ ordinal patterns per permutation type, satisfying the commonly adopted robustness condition $N/m! > 5$ (Bandt and Pompe, 2002; Kilpua et al., 2024). Larger embedding orders reduce this ratio; for $m = 4$ ($m! = 24$) the ratio drops to $\lfloor 80/24 \rfloor = 3$, approaching the reliability limit for the shortest admissible segments. Second, given the typical bin resolution of Konus-WIND light curves and the short pre-onset segments that characterize many events in the catalogue, $m = 3$ provides the best balance between ordinal-pattern resolution and statistical reliability across the full event population. The robustness of the results to variations in m and τ is confirmed in the sensitivity analysis (Appendix A, Table 3), where the key qualitative class-scaling patterns and the set of significant channel–descriptor combinations remain stable under $m \in \{3, 4\}$ and $\tau \in \{1, 2\}$.

Ordinal ties were handled using a stable ordering (stable sort) so that equal values were resolved deterministically. The ordinal distribution $P = \{p_i\}_{i=1}^{m!}$ was built from all embedded vectors in the segment. Normalized permutation entropy was computed as

$$H_{\text{perm}} = \frac{-\sum_{i=1}^{m!} p_i \ln p_i}{\ln(m!)}.$$

Statistical complexity was defined as

$$C_{JS} = H_{\text{perm}} \cdot Q_{JS},$$

where Q_{JS} is the Jensen–Shannon divergence between P and the uniform distribution, normalized by its maximum value for $m!$ states (Rosso et al., 2007).

Lempel–Ziv complexity and median binarization. To compute LZ, each standardized segment was binarized using the segment median as threshold (values above the median mapped to 1, otherwise 0). Normalized Lempel–Ziv complexity was then computed on the resulting binary string.

It is worth noting the relationship of these descriptors to the nature of hard X-ray flare emission. The Higuchi fractal dimension D_H measures multi-scale roughness: a higher D_H is expected when the count-rate profile consists of many superimposed, irregular burst components, as is typical of intense impulsive-phase emission (Benz, 2017; Holman et al., 2011). Normalised permutation entropy H_{perm} and statistical complexity C_{JS} together characterise ordinal structure: high H_{perm} with low C_{JS} indicates that the signal approaches a maximally disordered state with no dominant ordinal pattern, which can arise when many overlapping sub-second burst components are present simultaneously (Bandt and Pompe, 2002; Rosso et al., 2007). Normalised Lempel–Ziv complexity (LZ) quantifies how compressible a binarised version of the signal is: a signal dominated by long runs above or below its median — as may occur during a sustained burst peak — yields lower LZ than an irregular alternating sequence. Finally, Hjorth complexity measures effective dynamical bandwidth relative to a simple oscillator: it increases when the time derivative of the signal contains fine-scale structure relative to the signal itself, and is therefore sensitive to abrupt modulations that may accompany the most energetic impulsive-phase episodes (Hjorth, 1970; Morikawa and Nakamichi, 2023). These physical expectations provide the interpretive framework for the results reported in Section 3.

2.4. Event-level change definition

To focus on onset-related changes while controlling for event-to-event baseline variability, we computed for each event, channel, and descriptor an onset-associated difference:

$$\Delta = after - before,$$

where "before" and "after" refer to descriptor values computed on the pre- and post-onset segments, respectively.

2.5. Statistical analysis

All hypothesis tests were performed on event-level Δ values. Because the Δ distributions are not assumed to be Gaussian and can exhibit skewness and outliers, we used nonparametric tests throughout.

Between-class differences. For each channel–descriptor combination, we tested whether Δ differs across GOES classes using the Kruskal–Wallis test. When global differences were detected, we performed post hoc pairwise comparisons using the Mann–Whitney U test. We reported Cliff's δ as a nonparametric effect size for pairwise contrasts.

Multiple-testing control and reporting. To control false discoveries, we applied Benjamini–Hochberg false-discovery-rate correction to the families of tests within each channel. Results are reported using robust summaries (median and interquartile range, IQR) together with FDR-adjusted p-values.

Sensitivity analyses. We assessed robustness to segmentation choices, temporal coverage, and descriptor-parameter settings. First, we repeated the analysis using fixed-length windows of $N = 80$ bins immediately before and after onset; class-dependent effects remained significant in G1 and G2 for most descriptors; in G1, D_H, H_{perm}, and C_{JS} retain a monotonic C→M→X gradient, whereas normalized LZ complexity shows a C vs. (M, X) pattern with negligible M–X contrast (Cliff's $\delta = -0.11$, $p = 0.027$), indicating that the full monotonic gradient for this descriptor depends on longer post-onset segments, whereas in G3 no clear between-class discrimination was detectable under this onset-proximal window definition, with all five descriptors yielding non-significant or marginally significant KW tests (Supplementary Fig. 5). Second, we stratified events into three eras aligned with solar cycle boundaries (Hathaway, 2015): SC22-tail+SC23 (1994–2008; $n = 674$), SC24 (2009–2019; $n = 251$), and SC25 (2020–2025; $n = 209$); the class composition of each era is reported in Table 3 in Appendix A. Third, we varied ordinal-pattern parameters (m, τ), LZ binarization rule (median vs mean), z-score standardization (on/off), and ordinal tie handling; the set of significant channel–descriptor combinations and the key qualitative class-scaling patterns remained stable (Supplementary Table 4).

3. Results

We evaluated whether event-centered changes in geometric and complexity-based descriptors, defined as $\Delta = after - before$, show statistically detectable differences across GOES flare classes (C, M, X) in the three background-subtracted Konus-WIND channels (G1, G2, and G3). The descriptors considered are Higuchi fractal dimension, normalized permutation entropy, statistical complexity C_{JS}, normalized Lempel–Ziv complexity, and Hjorth complexity. All statistical analyses were conducted on event-level Δ values using nonparametric tests with false-discovery-rate (FDR) correction.

Key class-dependent patterns were stable under fixed-window segmentation, era stratification, and reasonable parameter variations (Appendix A, Figs. 5 and 6; Table 4).

3.1. Statistical overview of onset-related changes and class dependence

The analysis dataset comprises $n_C = 322$, $n_M = 641$, and $n_X = 178$ C-, M-, and X-class events per channel–descriptor combination (Tables 1 and 2). B-class events ($n_B = 5$) were excluded from all analyses prior to testing, as described in Section 2.2.

Across channels and descriptors, pre/post-onset differences were generally non-zero in most class-specific combinations, indicating that flare onset is associated with a systematic reorganization of signal structure. This broad onset effect is also visible in the heatmap representation (Fig. 3), where most class-wise median Δ values depart from zero across the three channels.

To determine whether the magnitude of this onset-related reorganization depends on flare class, we applied Kruskal–Wallis tests to event-level Δ values for each channel–descriptor combination (Table 1). Most combinations

Table 1
Event-level pre/post-onset changes ($\Delta = \mathrm{after} - \mathrm{before}$) summarized as median [IQR] for each GOES class and descriptor in the G1, G2, and G3 channels. Kruskal–Wallis p-values are FDR-corrected across channel-wise descriptor families. In all rows, the C/M/X sample sizes are $n = 322/641/178$. Asterisks indicate significance levels ($^{*}p < 0.05$, $^{**}p < 0.01$, $^{***}p < 0.001$).

Channel	Metric	C: median Δ [IQR]	M: median Δ [IQR]	X: median Δ [IQR]	$p_{\mathrm{KW,FDR}}$
G1	ΔC_{JS}	-2.08×10^{-4} [-4.28, -0.825]$\times10^{-4}$	-3.64×10^{-3} [-6.97, -1.73]$\times10^{-3}$	-0.006 [-0.015, -0.002]	$1.6\times10^{-14***}$
G1	Δ LZ	-0.444 [-0.651, -0.251]	-0.573 [-0.708, -0.352]	-0.562 [-0.727, -0.269]	0.001^{**}
G1	ΔH_{perm}	2.11×10^{-3} [0.838, 4.30]$\times10^{-3}$	3.73×10^{-3} [1.76, 7.22]$\times10^{-3}$	0.006 [0.002, 0.016]	$1.2\times10^{-14***}$
G1	ΔD_H	0.132 [0.058, 0.204]	0.215 [0.126, 0.305]	0.301 [0.167, 0.394]	$3.8\times10^{-32***}$
G1	Δ Hjorth	-1.55 [-2.50, -0.50]	-1.69 [-3.23, 0.57]	-0.26 [-5.58, 6.67]	0.062
G2	ΔC_{JS}	-1.86×10^{-4} [-1.97, 1.38]$\times10^{-3}$	-8.36×10^{-4} [-2.68, 0.464]$\times10^{-3}$	-1.10×10^{-3} [-3.10, 0.235]$\times10^{-3}$	$5.4\times10^{-6***}$
G2	Δ LZ	-0.145 [-0.300, -0.073]	-0.313 [-0.514, -0.151]	-0.492 [-0.728, -0.246]	$1.2\times10^{-26***}$
G2	ΔH_{perm}	1.80×10^{-4} [-1.42, 2.00]$\times10^{-3}$	8.34×10^{-4} [-0.482, 2.75]$\times10^{-3}$	1.13×10^{-3} [-0.221, 3.11]$\times10^{-3}$	$5.4\times10^{-6***}$
G2	ΔD_H	-0.069 [-0.104, -0.041]	-0.073 [-0.105, -0.038]	-0.085 [-0.143, -0.038]	0.024^{*}
G2	Δ Hjorth	-0.435 [-0.691, -0.021]	-0.099 [-0.563, 0.952]	1.89 [-0.38, 6.84]	$1.2\times10^{-21***}$
G3	ΔC_{JS}	0.015 [0.011, 0.018]	0.014 [0.010, 0.018]	0.013 [0.009, 0.017]	0.005^{**}
G3	Δ LZ	-0.082 [-0.114, -0.053]	-0.081 [-0.116, -0.045]	-0.113 [-0.209, -0.067]	$2.4\times10^{-7***}$
G3	ΔH_{perm}	-0.016 [-0.019, -0.012]	-0.015 [-0.018, -0.011]	-0.014 [-0.017, -0.009]	0.005^{**}
G3	ΔD_H	-0.104 [-0.130, -0.077]	-0.103 [-0.133, -0.073]	-0.105 [-0.136, -0.069]	0.373
G3	Δ Hjorth	0.016 [-0.038, 0.067]	0.030 [-0.033, 0.077]	0.062 [-0.006, 0.164]	$5.4\times10^{-7***}$

remained significant after FDR correction, showing that the onset-induced change is not only present but also class-dependent. Post hoc Mann–Whitney tests (Table 2) further show that the strongest differences are concentrated among the C, M, and X classes, especially in C–X and M–X contrasts, consistent with a graded increase in structural change as flare intensity increases.

The heatmap in Fig. 3 also reveals an important feature of the results: class dependence is channel- and descriptor-specific. Some descriptors show monotonic scaling with flare class in one channel but weak discrimination in another. Figure 4 presents all three channels simultaneously for each descriptor, providing a direct visual comparison of the channel-dependent scaling patterns.

Robustness to segmentation, temporal coverage, and parameter choices. To ensure that the reported class-dependent effects are not an artifact of segment length or a specific parameter setting, we carried out three complementary robustness checks (Appendix A). First, we repeated the full analysis using fixed-length onset-centered windows of $N = 80$ bins immediately before and after onset. Under this onset-proximal definition, all five descriptors remained significant in both G1 and G2, though in G1 the character of the dependence varies across descriptors: D_H, H_{perm}, and C_{JS} retain a monotonic C→M→X gradient, whereas normalized LZ complexity shows a C vs. (M, X) pattern with negligible M–X contrast, indicating that the full monotonic gradient for that descriptor depends on longer post-onset segments. In G3, no clear between-class discrimination was detectable under the fixed-window definition. This indicates that the main class-scaling signatures in G1 and G2 do not rely on long post-onset segments, while suggesting that class-dependent structure in G3 is weaker near onset or may require longer post-onset evolution to become apparent.

Second, we stratified events by solar cycle era (Table 3; see Section 2.5) and repeated the Kruskal–Wallis tests within each era (Appendix A, Fig. 6). In the two largest eras — SC22–SC23 ($n = 674$) and SC24 ($n = 251$) — the class-dependent signatures identified in the main analysis are broadly preserved: 14 of 15 and 12 of 15 channel–descriptor combinations, respectively, remained significant after FDR correction, corresponding to stability fractions of 0.93 and 0.80. In the SC25 era ($n = 209$), however, only 4 of 15 combinations remained significant (stability fraction 0.27). This reduction in SC25 is largely attributable to the small C-class sample in that era ($n_C = 29$), which limits statistical power for pairwise comparisons, rather than to a genuine absence of class-dependent structure. The C-class imbalance in SC25 reflects the early phase of the current solar cycle at the time of catalogue compilation, during which M and X-class events are disproportionately represented relative to the full population of flares (Hathaway,

Table 2
Significant post hoc pairwise comparisons of event-level Δ values (Mann–Whitney U tests, FDR-corrected). Only contrasts with $p_{\mathrm{FDR}} < 0.05$ are shown. For each channel–descriptor combination, the table reports class-wise medians, median differences, Cliff's δ effect sizes, and adjusted p-values. Asterisks indicate significance levels ($^{*}p < 0.05$, $^{**}p < 0.01$, $^{***}p < 0.001$).

Channel	Metric	Pair	Median (class 1)	Median (class 2)	Median diff (1-2)	Cliff's δ	p_{FDR}
G1	ΔC_{JS}	C–M	-2.08×10^{-3}	-3.64×10^{-3}	1.56×10^{-3}	0.274	$2.3\times10^{-11***}$
G1	ΔC_{JS}	C–X	-2.08×10^{-3}	-5.86×10^{-3}	3.77×10^{-3}	0.360	$8.2\times10^{-11***}$
G1	ΔC_{JS}	M–X	-3.64×10^{-3}	-5.86×10^{-3}	2.21×10^{-3}	0.172	$9.0\times10^{-4***}$
G1	Δ LZ	C–M	-0.444	-0.573	0.129	0.162	$2.4\times10^{-4***}$
G1	ΔH_{perm}	C–M	2.11×10^{-3}	3.73×10^{-3}	-1.63×10^{-3}	-0.276	$1.6\times10^{-11***}$
G1	ΔH_{perm}	C–X	2.11×10^{-3}	5.96×10^{-3}	-3.86×10^{-3}	-0.364	$4.8\times10^{-11***}$
G1	ΔH_{perm}	M–X	3.73×10^{-3}	5.96×10^{-3}	-2.23×10^{-3}	-0.176	$6.5\times10^{-4***}$
G1	ΔD_H	C–M	0.132	0.215	-0.083	-0.377	$3.6\times10^{-21***}$
G1	ΔD_H	C–X	0.132	0.301	-0.169	-0.576	$8.4\times10^{-26***}$
G1	ΔD_H	M–X	0.215	0.301	-0.086	-0.280	$2.2\times10^{-8***}$
G2	ΔC_{JS}	C–M	-1.86×10^{-4}	-8.36×10^{-4}	6.50×10^{-4}	0.186	$1.5\times10^{-5***}$
G2	ΔC_{JS}	C–X	-1.86×10^{-4}	-1.10×10^{-3}	9.16×10^{-4}	0.227	$8.1\times10^{-5***}$
G2	Δ LZ	C–M	-0.145	-0.313	0.168	0.347	$3.9\times10^{-18***}$
G2	Δ LZ	C–X	-0.145	-0.492	0.346	0.524	$1.8\times10^{-21***}$
G2	Δ LZ	M–X	-0.313	-0.492	0.179	0.259	$2.4\times10^{-7***}$
G2	ΔH_{perm}	C–M	1.80×10^{-4}	8.34×10^{-4}	-6.54×10^{-4}	-0.185	$1.6\times10^{-5***}$
G2	ΔH_{perm}	C–X	1.80×10^{-4}	1.13×10^{-3}	-9.45×10^{-4}	-0.226	$8.7\times10^{-5***}$
G2	Δ Hjorth	C–M	-0.435	-0.099	-0.336	-0.260	$1.3\times10^{-10***}$
G2	Δ Hjorth	C–X	-0.435	1.893	-2.327	-0.485	$1.5\times10^{-18***}$
G2	Δ Hjorth	M–X	-0.099	1.893	-1.991	-0.317	$1.8\times10^{-10***}$
G3	ΔC_{JS}	C–X	0.015	0.013	1.98×10^{-3}	0.194	0.002^{**}
G3	Δ LZ	C–X	-0.082	-0.113	0.031	0.272	$1.5\times10^{-6***}$
G3	Δ LZ	M–X	-0.081	-0.113	0.032	0.276	$1.1\times10^{-7***}$
G3	ΔH_{perm}	C–X	-0.016	-0.014	-2.20×10^{-3}	-0.196	0.002^{**}
G3	Δ Hjorth	C–X	0.016	0.062	-0.046	-0.290	$4.7\times10^{-7***}$
G3	Δ Hjorth	M–X	0.030	0.062	-0.032	-0.227	$1.0\times10^{-5***}$

2015). The core signatures in G1 (Higuchi fractal dimension, permutation entropy, and C_{JS}) and in G2 (Lempel–Ziv complexity) are retained in both SC22–SC23 and SC24, supporting the interpretation that these patterns reflect genuine population-level class scaling rather than era-specific instrumental or activity effects.

3.2. Channel-resolved signatures of flare-class scaling

The channel-resolved panels (Fig. 4), together with the summary and post hoc statistics (Tables 1 and 2), show that the three channels contribute complementary information about flare intensity.

In the G1 channel (see Fig. 4), the strongest and most coherent class-dependent behavior is observed in the Higuchi fractal dimension, normalized permutation entropy, and statistical complexity C_{JS}. The median change in Higuchi fractal dimension increases monotonically from C to M to X flares (0.132, 0.215, and 0.301, respectively), yielding the strongest global class effect in the study ($p_{\mathrm{KW,FDR}} \approx 3.8 \times 10^{-32}$). A similarly ordered trend is observed for normalized permutation entropy, whose median Δ increases from 2.11×10^{-3} (C) to 3.73×10^{-3} (M) and 5.96×10^{-3} (X). By contrast, statistical complexity C_{JS} becomes progressively more negative with flare class (-2.08×10^{-3}, -3.64×10^{-3}, and -5.86×10^{-3} for C, M, and X, respectively). The opposite-sign behavior of permutation entropy and C_{JS} is consistent with the coupled structure of the complexity–entropy framework. Together, these results indicate that stronger flares produce larger onset-related changes in both geometric roughness and ordinal organization in G1. In the same channel, normalized Lempel–Ziv complexity also shows a negative post-onset shift with class dependence, but with weaker pairwise separation than the fractal and ordinal descriptors, while Hjorth complexity exhibits broad dispersion and no statistically robust global class effect ($p_{\mathrm{KW,FDR}} = 0.062$).

The G2 channel (see Fig. 4) shows a different but equally informative pattern. Here, the clearest class discrimination is provided by normalized Lempel–Ziv complexity and Hjorth complexity. Normalized Lempel–Ziv complexity becomes increasingly more negative from C to M to X flares, with median Δ values of −0.145, −0.313, and −0.492, respectively, and significant pairwise separation among all C/M/X contrasts. Hjorth complexity shows an even more distinctive transition: the median change is negative for C flares (−0.435), close to zero for M flares (−0.099), and strongly positive for X flares (+1.89). This sign reversal and amplitude increase produce a marked class-dependent signature and are consistent with G2 being more sensitive to changes in temporal irregularity and dynamical structure in the most energetic events. The remaining descriptors in G2 also show statistically significant class dependence, but their median shifts are smaller in magnitude than the dominant G1 trends in fractal and ordinal descriptors.

In the G3 channel (see Fig. 4), onset-related changes remain evident, but class discrimination is weaker overall. The clearest example is the Higuchi fractal dimension, whose median Δ values are nearly identical across C, M, and X flares (approximately −0.104, −0.103, and −0.105, respectively), yielding no significant global class effect ($p_{\mathrm{KW,FDR}} = 0.373$). Nevertheless, G3 still retains class information in two descriptors: normalized LZ complexity shows stronger negative shifts for X-class flares than for C/M (C–X and M–X contrasts both significant), and Hjorth complexity yields a significant C–X contrast ($p_{\mathrm{FDR}} = 4.7 \times 10^{-7}$), driven primarily by the X-class events. These contrasts are predominantly C vs. X rather than a monotonic C→M→X gradient, which is consistent with the intermittent detection of >300 keV emission: at these energies, which probe the most energetic nonthermal electrons and are contaminated by the 511 keV positron annihilation line in the strongest events (Holman et al., 2011), the signal-to-noise ratio varies substantially across the population, and the between-class contrast is partially masked by dispersion from events with marginal emission.

3.3. Implications for flare characterization

The combined evidence from the statistical tests, summary tables, heatmap representation, and full class-scaling panels supports the central claim of this study: solar-flare classes can be characterized by channel-dependent changes in geometric and complexity-based descriptors computed around flare onset.

Three complementary channel roles emerge. First, G1 provides the strongest monotonic scaling with flare class, particularly in Higuchi fractal dimension, normalized permutation entropy, and statistical complexity C_{JS}. Second, G2 provides the strongest separation in normalized Lempel–Ziv complexity and Hjorth complexity, including a marked Hjorth-complexity transition in X-class flares. Third, G3 captures a clear and statistically robust onset-related reorganization but shows comparatively weaker separation among flare classes.

These findings suggest that multichannel Δ descriptors provide a compact statistical representation of onset-related temporal reorganization that differs across flare classes in a channel-dependent manner. While this work focuses on hypothesis testing and effect-size characterization rather than predictive modeling, the results motivate future studies evaluating classification performance under strict validation and sensitivity analyses.

4. Discussion

The results indicate that flare onset is accompanied by systematic changes in the temporal structure of Konus-WIND count-rate signals, and that the magnitude and direction of these changes depend on both GOES class and energy channel. In this sense, the event-level Δ descriptors quantify onset-related reorganization and exhibit channel-dependent class scaling.

A key point for interpretation is that the analyzed signals (G1, G2, G3) are photon count-rate channels from Konus-WIND and therefore primarily probe the radiative and particle-acceleration dynamics at the flare source (corona / chromosphere), rather than heliospheric particle transport itself (Lysenko et al., 2022; Lysenko, Svinkin, Frederiks, Ridnaia, Tsvetkova and Ulanov, 2025; Fletcher, 2024; Benz, 2017; Holman et al., 2011). Thus, the observed complexity changes should be interpreted first as signatures of impulsive-phase temporal organization, spectral hardness evolution, and intermittency of energy release. Their possible heliospheric implications (e.g., association with CME/SEP productivity) are best treated as a secondary connection and require additional event information (Desai and Giacalone, 2016; Papaioannou, Sandberg, Anastasiadis, Kouloumvakos, Georgoulis, Tziotziou, Tsiropoula, Jiggens and Hilgers, 2016).

4.1. Physical interpretation of channel-dependent complexity changes

The strongest monotonic class scaling in the G1 channel, particularly for Higuchi fractal dimension, permutation entropy, and statistical complexity C_{JS}, suggests that lower-energy high-energy emission (within the Konus-WIND triggered band structure) is especially sensitive to how the flare onset reorganizes the temporal pattern of burst emission. The positive ΔD_H trend in G1 (increasing from C to M to X) is consistent with a post-onset increase in multiscale roughness or irregularity of the signal, which may reflect stronger intermittency, pulse overlap, and fragmented energy release in more intense flares (Benz, 2017; Fletcher, 2024; Schrijver, 2009). In physical terms, stronger flares may involve more intense and/or more temporally fragmented acceleration and heating episodes, which could manifest as richer fine-scale structure in the observed count-rate profiles.

The class-dependent complexity changes in the G1 channel (~20–80 keV) and G2 channel (~80–300 keV) are physically connected to the chromospheric evaporation process: accelerated nonthermal electrons precipitate into the chromosphere, deposit energy, drive rapid heating and hydrodynamic expansion, and fill coronal loops with hot plasma that produces the soft X-ray emission detected by GOES (Holman et al., 2011; Dennis, 1985). The temporal derivative of this soft X-ray flux approximately tracks the hard X-ray count rate (the Neupert effect; Neupert 1968; Crannell, Frost, Saba, Maetzler and Ohki 1978), but the relationship is statistical rather than deterministic: substantial event-by-event deviations are well documented (Holman et al., 2011; Fletcher et al., 2011), and the Konus-WIND G1 band samples primarily nonthermal bremsstrahlung contributions not fully captured by the thermal GOES proxy. The monotonic increase of ΔD_H and $\Delta H_{\rm perm}$ from C to M to X flares in G1 therefore reflects the growing temporal fragmentation and burst overlap of the accelerated electron population as flare energy release intensifies, rather than a simple rescaling of the SXR derivative.

The paired behavior of $\Delta H_{\rm perm}$ and ΔC_{JS} in G1 (~20–80 keV) is also notable. As flare class increases, permutation entropy tends to increase while C_{JS} becomes more negative (i.e., decreases relative to the pre-onset baseline). Within the complexity–entropy framework, this joint trend is consistent with a shift of the ordinal pattern distribution toward higher entropy and lower disequilibrium after onset (Bandt and Pompe, 2002; Rosso et al., 2007, 2012). A physically plausible interpretation is that stronger flares produce a broader and more rapidly changing superposition of elementary emission structures (bursts, spikes, and subpulses), which increases ordinal diversity even as the post-onset signal becomes less similar to the pre-onset structured baseline. At the same time, this interpretation should be treated with caution because $H_{\rm perm}$ and C_{JS} are sensitive to symbolization choices (embedding order, delay, tie handling) and to the effective signal-to-noise ratio.

In contrast, G2 (~80–300 keV) exhibits its strongest class separation in normalized Lempel–Ziv and Hjorth complexity, with a particularly distinctive Hjorth-complexity increase for X-class flares. This pattern suggests that the intermediate-energy channel is especially responsive to changes in the signal's dynamical bandwidth and local derivative structure during the impulsive phase. Hjorth complexity increases when the time series departs from a simple oscillatory pattern and develops richer local fluctuation structure; the marked positive Δ values for X-class events in G2 are therefore consistent with more abrupt temporal modulation and stronger high-frequency variability in the most energetic flares (Morikawa and Nakamichi, 2023; Zimovets et al., 2021; Holman et al., 2011). The concurrent class-dependent decrease in normalized Lempel–Ziv complexity in G2 may appear counterintuitive at first, but it can be reconciled with the Hjorth result if stronger flares produce more structured but more compressible symbolic sequences (e.g., repeated pulse motifs, threshold-dominated segments, or long runs after binarization), rather than purely stochastic fluctuations. This emphasizes that different complexity measures capture different aspects of temporal organization and should not be interpreted as interchangeable proxies.

The G3 channel (~300–1200 keV) shows a robust onset response but weaker class discrimination overall, especially for Higuchi fractal dimension, which remains nearly class-invariant. A likely explanation is that the highest-energy channel is affected more strongly by limited counting statistics, event-to-event sparsity, and greater heterogeneity in detectability across flare classes, which can attenuate class-dependent trends in shape descriptors. In this regime, the onset signal may still be strong enough to produce systematic pre/post differences, but the between-class contrast becomes partially masked by dispersion. The fact that G3 still retains class information in selected descriptors (notably Lempel–Ziv and Hjorth complexity) suggests that some aspects of temporal organization remain detectable even when fractal scaling is less stable.

4.2. Methodological implications, caveats, and next steps

Several methodological aspects are important for interpreting the physical meaning of the reported complexity changes. First, background subtraction and low-count behavior can strongly affect ordinal and symbolic metrics, particularly in higher-energy channels. Tie handling, binarization strategy (for Lempel–Ziv), and preprocessing choices can alter absolute metric values and, in some cases, even the sign of small pre/post differences. The fact that the strongest class trends remain statistically robust across many channel–descriptor combinations is encouraging, but a sensitivity analysis to preprocessing choices is essential for physical confidence.

Second, even within the C/M/X regime, GOES class aggregates events with potentially different durations, morphologies, spectral evolution, and magnetic environments, so that the dispersion seen in the descriptors likely reflects real physical heterogeneity rather than measurement noise alone. The conclusions of this work should therefore be interpreted as strongest for the C/M/X regime.

Finally, the present results support a multichannel and multi-descriptor strategy for flare characterization. The channel-specific behavior indicates that no single metric is sufficient to summarize onset dynamics across the full flare population. Instead, the strongest path forward is a physically informed feature set combining: (i) fractal and ordinal descriptors (especially in G1), (ii) dynamical/symbolic complexity descriptors (especially in G2), and (iii) selective high-energy descriptors from G3. Such a representation motivates subsequent predictive studies and future tests of linkage between flare temporal structure, CME properties, and SEP productivity using additional event metadata.

Beyond the statistical scope of the present study, the channel complementarity found here may provide a physically informed feature set for future integration with CME and SEP metadata: fractal and ordinal descriptors from G1 characterise the thermal-to-impulsive transition; symbolic and waveform descriptors from G2 capture the intensity of nonthermal acceleration; and G3 contributions, when detectable, may serve as a proxy for the most energetic electron populations linked to SEP production (Shih et al., 2009; Desai and Giacalone, 2016).

5. Conclusions

In this work we carried out an event-centered, pre/post-onset analysis of Konus-WIND solar-flare time series to evaluate whether onset-associated changes in geometric and complexity-based descriptors are statistically associated with GOES flare class. Using paired differences defined as $\Delta = \mathtt{after} - \mathtt{before}$ and computed independently for each energy channel, we find that flare onset is accompanied by systematic changes in temporal-structure descriptors across the Konus-WIND event population. These onset-associated shifts are evident in robust distributional summaries (median and interquartile range) and remain detectable under nonparametric inference with explicit false-discovery-rate control.

The magnitude of the onset-associated complexity change scales with GOES class in a channel-dependent manner that reflects the underlying impulsive-phase physics. In the G1 channel (∼20–80 keV), the Higuchi fractal dimension, permutation entropy, and C_{JS} increase monotonically from C to M to X flares, consistent with growing temporal fragmentation of the nonthermal electron precipitation as energy release intensifies. In the G2 channel (∼80–300 keV), normalized LZ complexity and Hjorth complexity provide the clearest class discrimination, including a sign reversal in Hjorth complexity for X-class events that indicates a qualitative change in the dynamical bandwidth of the emission. In the G3 channel (∼300–1200 keV), class discrimination is weaker and concentrated in C vs. X contrasts for LZ complexity and Hjorth complexity, consistent with the intermittent nature of >300 keV emission across the flare population.

We establish population-level statistical associations between GOES class and onset-centered temporal-structure descriptors in Konus-WIND channels, but we do not claim a direct mapping to specific microphysical mechanisms or to heliospheric impacts without additional event metadata. Future work will evaluate predictive performance using multichannel Δ feature sets under strict validation and class-imbalance handling, and will investigate how the identified temporal-structure signatures relate to additional physical covariates such as flare duration, impulsiveness, spectral hardness evolution, and eruptive context.

A. Sensitivity analyses and robustness checks

To assess the robustness of the main results to segmentation choices and descriptor-parameter settings, we conducted several complementary sensitivity and robustness analyses. First, we repeated the full pipeline using fixed-length onset-centered windows of $N = 80$ bins immediately before and after onset, in order to reduce potential confounding from unequal segment lengths and long-duration post-onset evolution. Second, we evaluated parameter sensitivity by varying ordinal-pattern settings (m, τ), Lempel–Ziv (LZ) binarization rule, z-score standardization, and ordinal tie handling. Unless otherwise stated, all tests reported below use the same nonparametric inference and Benjamini–Hochberg false-discovery-rate (FDR) control as in the main text.

Table 3
Distribution of Konus-WIND flare events by solar cycle era and GOES class used in the temporal stability analysis. Era boundaries follow official NOAA/SIDC solar cycle minimum dates (Hathaway 2015). B-class events ($n_B = 5$, all in SC22–SC23) are excluded from all statistical analyses.

Era	C	M	X	Total (C/M/X)
SC22–SC23 (1994–2008)	220	363	91	674
SC24 (2009–2019)	71	143	37	251
SC25 (2020–2025)	29	131	49	209
Total	320	637	177	1,134

A.1. Fixed-length onset-centered windows

Figure 5 shows class-wise median $\Delta = \mathtt{after} - \mathtt{before}$ values computed using fixed-length windows ($N = 80$ bins) before and after onset. Under this onset-proximal definition, G1 retains significant class dependence in all five descriptors, but the character of the dependence varies: D_H, H_{perm}, and C_{JS} maintain a monotonic C→M→X gradient, whereas normalized LZ complexity shows a C vs. (M, X) pattern with negligible M–X contrast (Cliff's $\delta = -0.11$), and Hjorth complexity shows broad class separation without a monotonic trend. In G2, all five descriptors remain significant. In G3, no clear between-class discrimination was detectable, with all five descriptors yielding non-significant or marginal KW tests. This indicates that the core class-scaling signatures in G1 and G2 are not driven solely by variable segment length, while confirming that class-dependent structure in G3 requires longer post-onset evolution to become apparent.

One notable difference between the fixed-window and full-segment results deserves explicit comment. In the main analysis, the G2 Hjorth complexity shows a sign reversal across flare classes, with a median Δ that is negative for C-class events (-0.435), near zero for M-class (-0.099), and strongly positive for X-class events ($+1.89$). Under fixed-length windows of $N = 80$ bins, however, this sign reversal disappears: the median Δ remains negative and monotonically decreasing across classes (-0.514, -0.564, -0.611 for C, M, and X, respectively; Fig. 5). This discrepancy is not a contradiction but rather an informative feature of the data. It indicates that the distinctive Hjorth-complexity transition observed for X-class flares in the full-segment analysis is a temporally extended phenomenon: the strong positive shift in dynamical bandwidth characteristic of X-class events in G2 develops progressively over the post-onset evolution and is not yet fully expressed in the first $N = 80$ bins immediately following trigger. Physically, this is consistent with a gradual intensification of high-frequency modulation in the most energetic events, driven by the sustained and increasingly fragmented character of particle acceleration during the extended impulsive phase (Holman et al., 2011; Zimovets et al., 2021). The fixed-window result thus provides a complementary, onset-proximal view, while the full-segment result captures the cumulative reorganization of temporal structure over the complete post-onset interval.

Figure 6 shows the Kruskal–Wallis FDR-corrected p-values as $-\log_{10}(p_{\mathrm{FDR}})$ for each channel–descriptor combination, stratified by solar cycle era. The heatmaps confirm that the dominant signatures in G1 (particularly ΔD_H and ΔH_{perm}) and G2 (particularly Δ LZ complexity and Δ Hjorth complexity) are consistently present in SC22–SC23 and SC24. The reduced significance in SC25 is concentrated in descriptors and channels where class discrimination requires adequate C-class representation; the M–X contrasts, which are less affected by the small n_C in SC25, remain directionally consistent with the main results.

A.2. Sensitivity to descriptor-parameter settings

To test whether the main conclusions depend on a single parameter choice, we repeated the analysis under a small grid of reasonable settings (Table 4), including variations of ordinal embedding (m, τ), LZ binarization (median vs mean), z-score standardization (on/off), and ordinal tie handling (stable vs jitter). We summarize stability relative to the baseline setting used in the main text in terms of (i) the number of significant Kruskal–Wallis tests across the 3×5 channel–descriptor combinations, (ii) the Jaccard similarity of the significant-test set relative to baseline, and (iii) boolean checks of the key qualitative patterns emphasized in the main text (monotonic G1 scaling in D_H and H_{perm}, monotonic G1 decrease in C_{JS}, monotonic G2 decrease in LZ, and the sign transition in G2 Hjorth complexity). Across the tested grid, the significant-test set and the qualitative class-scaling patterns remained stable, supporting the robustness of the main findings to reasonable parameter choices.

Table 4
Parameter-sensitivity summary relative to the baseline setting used in the main text. n_{sig} is the number of channel–descriptor Kruskal–Wallis tests (out of 15) that remain significant after FDR correction. "Jaccard" denotes the overlap of the significant-test set with the baseline. The remaining columns report whether the key qualitative patterns emphasized in the main text are preserved under each setting (Yes/No). For the Hjorth check, "jump" denotes $C < 0$ and $X > 0$ in the G2 Hjorth-complexity median Δ.

Setting	n_{sig} (of 15)	Jaccard	G1: $D_H \uparrow$	G1: $H_{\text{perm}} \uparrow$	G1: $C_{JS} \downarrow$	G2: LZ↓	G2: Hjorth jump
Baseline: m=3, τ=1; LZ=median; z-score on; ties stable	13	1.00	Yes	Yes	Yes	Yes	Yes
m=4, τ=1 (others baseline)	13	1.00	Yes	Yes	Yes	Yes	Yes
m=3, τ=2 (others baseline)	13	1.00	Yes	Yes	Yes	Yes	Yes
m=4, τ=2 (others baseline)	11	0.85	Yes	Yes	Yes	Yes	Yes
LZ threshold = mean (others baseline)	13	1.00	Yes	Yes	Yes	Yes	Yes
z-score off (others baseline)	13	1.00	Yes	Yes	Yes	Yes	Yes
ties = jitter (others baseline)	11	0.85	Yes	Yes	Yes	Yes	Yes

Table 5
G3 signal-quality subanalysis: Kruskal–Wallis FDR-corrected p-values for the full G3 sample and the subset restricted to events with $\text{SNR}_{G3} \geq 3.0$. The pattern of significant ($p_{\text{FDR}} < 0.05$, indicated by *) and non-significant results is identical across both subsets.

Metric	All G3 ($n = 1{,}156$)	SNR≥3 ($n = 1{,}139$)
ΔC_{JS}	$1.9 \times 10^{-3**}$	$3.5 \times 10^{-3**}$
Δ LZ complexity	$1.9 \times 10^{-7***}$	$1.4 \times 10^{-7***}$
ΔH_{perm}	$1.9 \times 10^{-3**}$	$3.5 \times 10^{-3**}$
ΔD_H (Higuchi)	0.990	0.988
Δ Hjorth complexity	$4.4 \times 10^{-7***}$	$1.8 \times 10^{-7***}$

A.3. G3 signal-quality subanalysis

To complement the fixed-window and parameter-sensitivity checks, we repeated the G3 class-dependence tests restricting the analysis to events with a pronounced signal above 300 keV, as defined by $\text{SNR}_{G3} \geq 3.0$ (Eq. 1, Section 2.2). Of the 1,156 events in the full catalogue, 1,152 (99.7%) met this criterion in terms of the SNR flag computed during extraction. After applying the minimum-length requirement ($n_{\min} = 80$) and building the delta table, the strong-signal subset comprised $n = 1{,}139$ events, representing 98.5% of the full G3 delta sample ($n = 1{,}156$).

Table 5 reports the Kruskal–Wallis FDR-corrected p-values for both the full and the strong-signal-only G3 subsets. The pattern of significant and non-significant channel–descriptor combinations is identical across both subsets: LZ complexity, Hjorth complexity, C_{JS}, and H_{perm} remain significant, while Higuchi fractal dimension remains non-significant in both. The high overlap between the two subsets (Jaccard = 1.00 on the significant-test set) confirms that the G3 results are not driven by low-SNR events and that the negligible fraction of events without pronounced >300 keV emission (< 0.3%) has no meaningful effect on the class-dependent complexity signatures.

A.4. Robustness to Konus-WIND trigger lag

The Konus-WIND trigger time follows the GOES soft X-ray begin time by a median of 248 s across the full sample (see Section 2.2). To confirm that this lag does not confound the class-dependent results, we performed two complementary checks.

First, we computed Spearman rank correlations between the trigger lag and Δ for each channel–descriptor combination. In G2 and G3, all but two correlations had $|\rho| < 0.15$, indicating that the trigger lag is not a meaningful confounder in these channels. In G1, moderate correlations were observed ($|\rho| \approx 0.24$–0.33); these reflect the collinearity between lag and GOES class (X-class events have both larger lags and larger complexity changes), rather than a direct causal role of the lag (Fig. 7).

Second, we stratified events by trigger lag into a *fast-trigger* group (lag ≤ 300 s; $n = 688$, C:268/M:373/X:70) and a *slow-trigger* group (lag > 300 s; $n = 450$, C:68/M:285/X:110) and repeated the Kruskal–Wallis tests within each group. The five primary descriptors emphasised in this paper are significant in both groups: in G1, D_H, H_{perm}, and C_{JS} each yield $p_{\text{FDR}} < 0.001$ regardless of trigger timing; in G2, LZ complexity and Hjorth complexity are similarly robust ($p_{\text{FDR}} < 0.001$ in both groups). Three secondary descriptors (ΔLZ in G1, ΔHjorth in G1, and ΔD_H in G2) lose significance in the slow-trigger group, likely due to the reduced C-class sample ($n_C = 68$). The stability fraction decreases from 14/15 (fast) to 9/15 (slow), but the qualitative pattern of the main results is preserved throughout.

CRediT authorship contribution statement

D. Sierra-Porta: Conceptualization, Methodology, Software, Validation, Formal analysis, Investigation, Resources, Data Curation, Writing - Original Draft, Writing - Review & Editing, Visualization, Supervision.. **J. D. Pérez-Navarro:** Methodology, Software. **J. D. Petro-Ramos:** Methodology, Software, Validation, Data Curation.

References

Aschwanden, M.J., Crosby, N.B., Dimitropoulou, M., Georgoulis, M.K., Hergarten, S., McAteer, J., Milovanov, A.V., Mineshige, S., Morales, L., Nishizuka, N., et al., 2016. 25 years of self-organized criticality: solar and astrophysics. Space Science Reviews 198, 47–166. doi:10.1007/s11214-014-0054-6.

Bandt, C., Pompe, B., 2002. Permutation entropy: a natural complexity measure for time series. Physical review letters 88, 174102. doi:10.1103/PhysRevLett.88.174102.

Benjamini, Y., Hochberg, Y., 1995. Controlling the false discovery rate: a practical and powerful approach to multiple testing. Journal of the Royal Statistical Society: Series B 57, 289–300. doi:10.1111/j.2517-6161.1995.tb02031.x.

Benz, A.O., 2017. Flare observations. Living reviews in solar physics 14, 2. doi:10.1007/s41116-016-0004-3.

Carrizales-Velázquez, C., Donner, R.V., Guzmán-Vargas, L., 2021. Generalization of Higuchi's fractal dimension for multifractal analysis of time series with limited length. Chaos, Solitons & Fractals 144, 110603. doi:10.1016/j.chaos.2021.110603.

Cliver, E.W., Schrijver, C.J., Shibata, K., Usoskin, I.G., 2022. Extreme solar events. Living Reviews in Solar Physics 19, 2. doi:10.1007/s41116-022-00033-8.

Crannell, C.J., Frost, K.J., Saba, J.L., Maetzler, C., Ohki, K., 1978. Impulsive solar x-ray bursts. Astrophysical Journal 223, 620–627. doi:10.1086/156297.

Dennis, B.R., 1985. Solar hard X-ray bursts. Solar Physics 100, 465–490. doi:10.1007/BF00158441.

Desai, M., Giacalone, J., 2016. Large gradual solar energetic particle events. Living Reviews in Solar Physics 13, 3. doi:10.1007/s41116-016-0002-5.

Fletcher, L., 2024. Solar flare spectroscopy. Annual Review of Astronomy and Astrophysics 62, 437–474. doi:10.1146/annurev-astro-052920-010547.

Fletcher, L., Dennis, B.R., Hudson, H.S., Krucker, S., Phillips, K., Veronig, A., Battaglia, M., Bone, L., Caspi, A., Chen, Q., et al., 2011. An observational overview of solar flares. Space science reviews 159, 19. doi:10.1007/s11214-010-9701-8.

Hathaway, D.H., 2015. The solar cycle. Living reviews in solar physics 12, 4. doi:10.1007/lrsp-2015-4.

Higuchi, T., 1988. Approach to an irregular time series on the basis of the fractal theory. Physica D: Nonlinear Phenomena 31, 277–283. doi:10.1016/0167-2789(88)90081-4.

Hjorth, B., 1970. EEG analysis based on time domain properties. Electroencephalography and Clinical Neurophysiology 29, 306–310. doi:10.1016/0013-4694(70)90143-4.

Holman, G.D., Aschwanden, M.J., Aurass, H., Battaglia, M., Grigis, P.C., Kontar, E.P., Liu, W., Saint-Hilaire, P., Zharkova, V.V., 2011. Implications of x-ray observations for electron acceleration and propagation in solar flares. Space science reviews 159, 107. doi:10.1007/s11214-010-9680-9.

Kilpua, E.K.J., Good, S., Ala-Lahti, M., Osmane, A., Koikkalainen, V., 2024. Permutation entropy and complexity analysis of large-scale solar wind structures and streams. Annales Geophysicae 42, 163–177. doi:10.5194/angeo-42-163-2024.

Lempel, A., Ziv, J., 1976. On the complexity of finite sequences. IEEE Transactions on Information Theory 22, 75–81. doi:10.1109/TIT.1976.1055501.

Lu, E.T., Hamilton, R.J., 1991. Avalanches and the distribution of solar flares. The Astrophysical Journal 380, L89. doi:10.1086/186180.

Lysenko, A., Ulanov, M., Kuznetsov, A., Fleishman, G., Frederiks, D., Kashapova, L., Sokolova, Z.Y., Svinkin, D., Tsvetkova, A., 2022. Kw-sun: the konus-wind solar flare database in hard x-ray and soft gamma-ray ranges. The Astrophysical Journal Supplement Series 262, 32. doi:10.3847/1538-4365/ac8b87.

Lysenko, A.L., Svinkin, D.S., Frederiks, D.D., Ridnaia, A.V., Tsvetkova, A.E., Ulanov, M.V., 2025. The third konus-wind catalogue of short gamma-ray bursts. Publications of the Astronomical Society of Australia 42, e063. doi:10.1017/pasa.2025.10027.

Morikawa, M., Nakamichi, A., 2023. Solar flare 1/f fluctuations from amplitude-modulated five-minute oscillation. Entropy 25, 1593. doi:10.3390/e25121593.

Neupert, W.M., 1968. Comparison of solar x-ray line emission with microwave emission during flares. Astrophysical Journal 153, L59. doi:10.1086/180220.

Papaioannou, A., Sandberg, I., Anastasiadis, A., Kouloumvakos, A., Georgoulis, M.K., Tziotziou, K., Tsiropoula, G., Jiggens, P., Hilgers, A., 2016. Solar flares, coronal mass ejections and solar energetic particle event characteristics. Journal of Space Weather and Space Climate 6, A42. doi:10.1051/swsc/2016035.

Rosso, O.A., Carpi, L.C., Saco, P.M., Ravetti, M.G., Plastino, A., Larrondo, H.A., 2012. Causality and the entropy–complexity plane: Robustness and missing ordinal patterns. Physica A: Statistical Mechanics and its Applications 391, 42–55. doi:10.1016/j.physa.2011.07.030.

Rosso, O.A., Larrondo, H., Martin, M.T., Plastino, A., Fuentes, M.A., 2007. Distinguishing noise from chaos. Physical review letters 99, 154102. doi:10.1103/PhysRevLett.99.154102.

Schrijver, C.J., 2009. Driving major solar flares and eruptions: A review. Advances in Space Research 43, 739–755. doi:10.1016/j.asr.2008.11.004.

Shih, A., Lin, R., Smith, D., 2009. Rhessi observations of the proportional acceleration of relativistic> 0.3 mev electrons and> 30 mev protons in solar flares. The Astrophysical Journal 698, L152–L157. doi:10.1088/0004-637X/698/2/L152.

Veronig, A., Temmer, M., Hanslmeier, A., Otruba, W., Messerotti, M., 2002. Temporal aspects and frequency distributions of solar soft X-ray flares. Astronomy & Astrophysics 382, 1070–1080. doi:10.1051/0004-6361:20011694.

Wanliss, J.A., Wanliss, G.E., 2022. Efficient calculation of fractal properties via the Higuchi method. Nonlinear Dynamics 109, 2893–2904. doi:10.1007/s11071-022-07353-2.

Weck, P.J., Schaffner, D.A., Brown, M.R., Wicks, R.T., 2015. Permutation entropy and statistical complexity analysis of turbulence in laboratory plasmas and the solar wind. Physical Review E 91, 023101. doi:10.1103/PhysRevE.91.023101.

Zimovets, I., McLaughlin, J., Srivastava, A., Kolotkov, D., Kuznetsov, A., Kupriyanova, E., Cho, I.H., Inglis, A., Reale, F., Pascoe, D., et al., 2021. Quasi-periodic pulsations in solar and stellar flares: a review of underpinning physical mechanisms and their predicted observational signatures. Space Science Reviews 217, 66. doi:10.1007/s11214-021-00840-9.

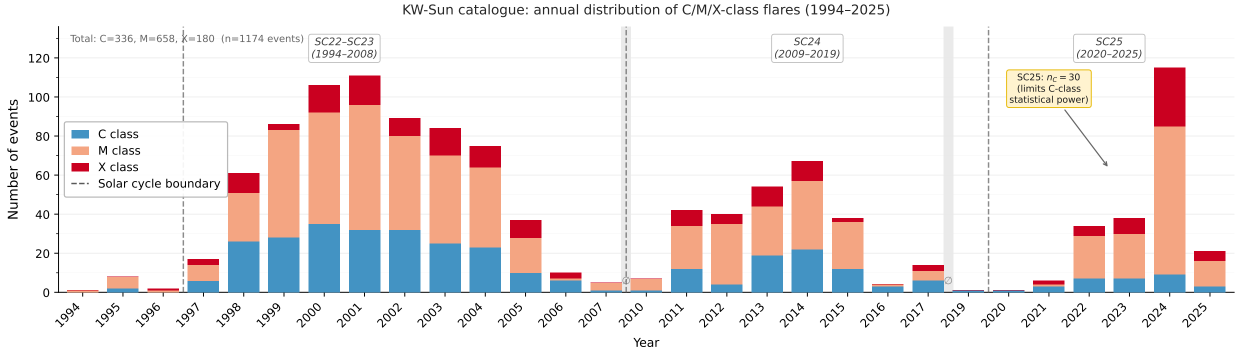

Figure 1: Annual distribution of C-, M-, and X-class Konus-WIND flare events used in this study (B-class events excluded). The dataset spans 1994–2025 across three solar cycles. Gaps in coverage (e.g., 2008–2009, 2018–2019) reflect periods of reduced detection near solar minima. The underrepresentation of C-class events in the SC25 era (2020–2025, $n_C = 29$) reflects the rising phase of the current solar cycle and limits statistical power for C-class contrasts in that era.

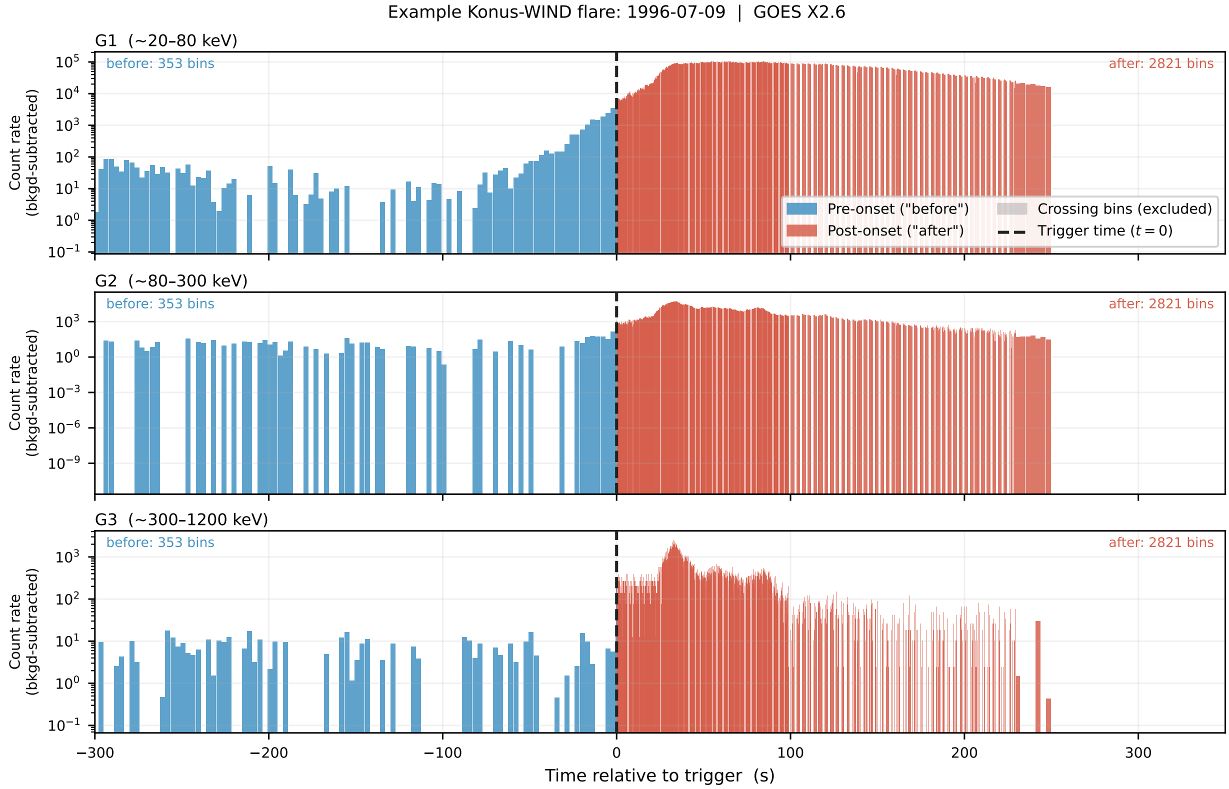

Figure 2: Illustration of the pre/post-onset segmentation applied to a representative Konus-WIND flare (1996 July 9, GOES X2.6). Background-subtracted count rates are shown for all three energy channels: G1 (~20–80 keV, top), G2 (~80–300 keV, middle), and G3 (~300–1200 keV, bottom). Blue bars indicate bins assigned to the pre-onset segment ($t_1 < 0$ and $t_2 < 0$); red bars indicate post-onset bins ($t_1 \geq 0$ and $t_2 \geq 0$). The single bin crossing the trigger time ($t_1 < 0 \leq t_2$, grey) is excluded from all descriptor calculations. The dashed vertical line marks the trigger time ($t = 0$). Complexity and geometric descriptors are computed independently on the pre- and post-onset segments of each channel, and the onset-associated change is defined as $\Delta = \mathrm{after} - \mathrm{before}$. Bin counts shown in the upper corners of each panel illustrate the variable segment lengths across channels that motivate the minimum-length criterion ($n_{\mathrm{min}} = 80$ valid samples per segment). Note that the count-rate axis is shown on a logarithmic scale to accommodate the large dynamic range of the signal across pre- and post-onset phases.

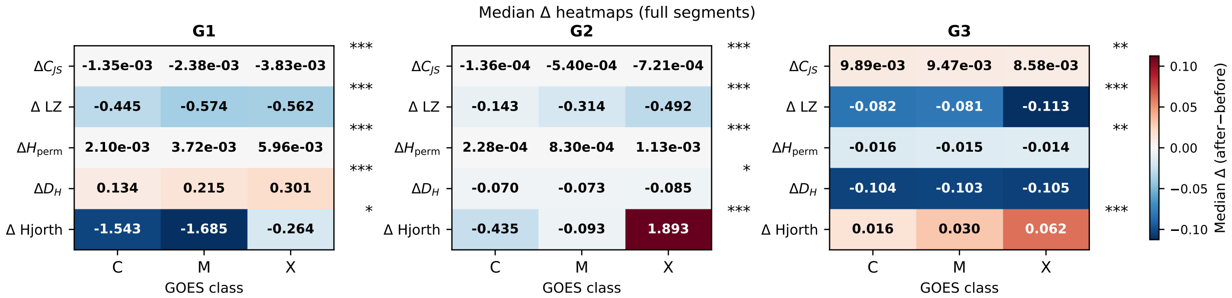

Figure 3: Class-wise median event-level changes ($\Delta = \text{after} - \text{before}$) in geometric and complexity-based descriptors across the three background-subtracted Konus-WIND channels (G1, G2, and G3). Rows correspond to descriptors and columns to GOES classes (C, M, X). Cell values report the median Δ, and the diverging color scale is centered at zero. Asterisks next to each descriptor indicate the significance of the Kruskal–Wallis test across classes after FDR correction ($^*p < 0.05$, $^* * p < 0.01$, $^* ** p < 0.001$). The heatmap summarizes the channel-dependent class scaling, highlighting strong monotonic trends in G1 and pronounced dynamic-complexity separation in G2.

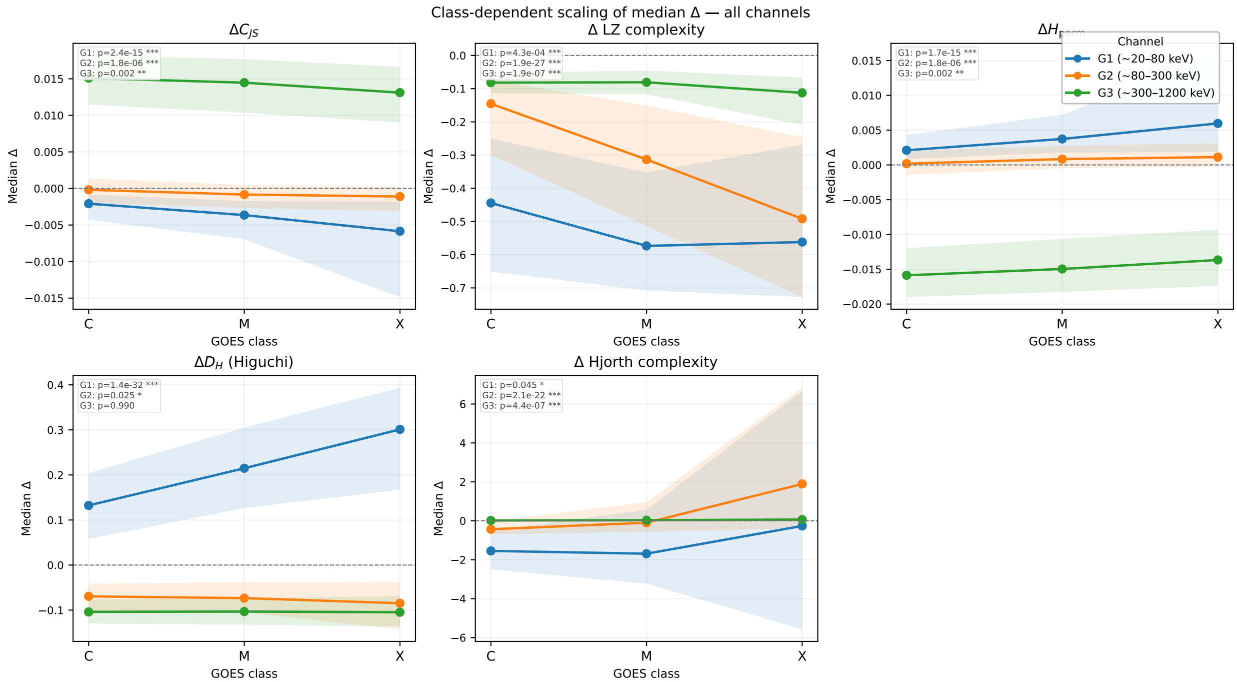

Figure 4: Combined class-scaling panel for all three Konus-WIND channels. Each subplot shows the class-wise median Δ for one descriptor (with IQR bands) across G1 (~20–80 keV, blue), G2 (~80–300 keV, orange), and G3 (~300–1200 keV, green). Inset text reports the FDR-corrected Kruskal–Wallis p-value for each channel. The complementary roles of the three channels are visible simultaneously: G1 shows monotonic C→M→X scaling in D_H, H_{perm}, and C_{JS}; G2 shows the strongest discrimination in LZ complexity and Hjorth complexity; G3 retains useful class information only in LZ and Hjorth, primarily in the C vs. X contrast.

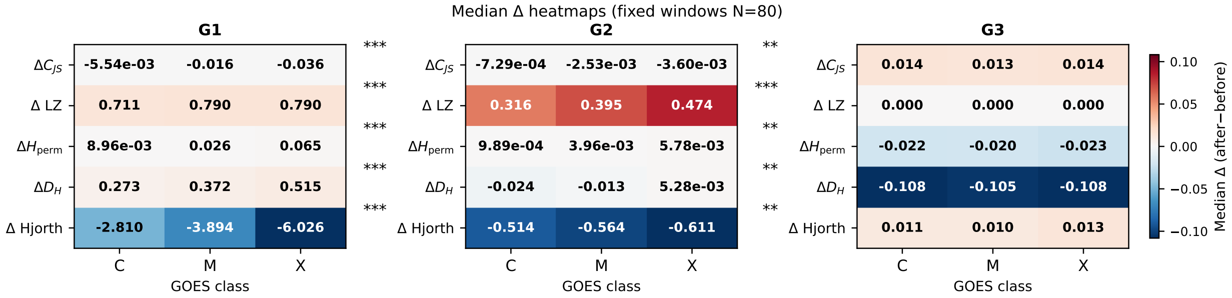

Figure 5: Median Δ heatmaps computed using fixed-length onset-centered windows ($N = 80$ bins before and $N = 80$ bins after onset) for the three Konus-WIND channels. Rows correspond to descriptors and columns to GOES classes (C, M, X). Cell values report class-wise median Δ, and asterisks indicate Kruskal–Wallis significance across classes after FDR correction ($^{*}p < 0.05$, $^{*}*\ p < 0.01$, $^{*}**\ p < 0.001$). Under this onset-proximal definition, class-dependent effects remain significant in G1 and G2 for most descriptors, while no clear between-class discrimination was detectable in G3.

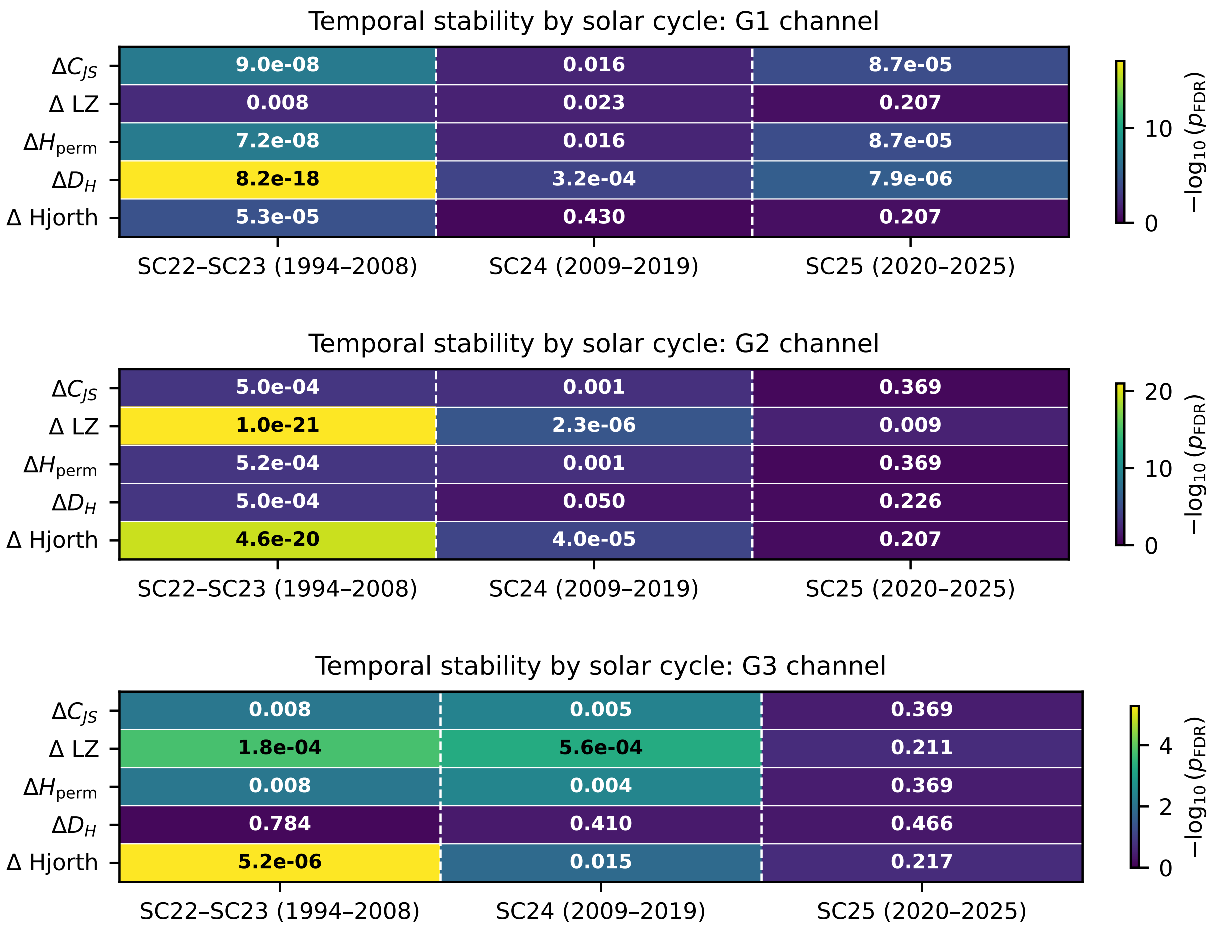

Figure 6: Temporal stability of Kruskal–Wallis class-dependence tests by solar cycle era. Each panel shows $-\log_{10}(p_{\mathrm{FDR}})$ for each channel–descriptor combination (rows) across the three eras aligned with solar cycle boundaries (columns). Era sample sizes: SC22–SC23 ($n = 674$), SC24 ($n = 251$), SC25 ($n = 209$). Cell values report the FDR-corrected p-value. Higher values (darker cells) indicate stronger and more stable class dependence. The reduced significance in SC25 is primarily attributable to the small C-class sample in that era ($n_C = 29$), which limits statistical power, rather than to a genuine absence of class-dependent structure. Core signatures in G1 and G2 are preserved in SC22–SC23 and SC24.

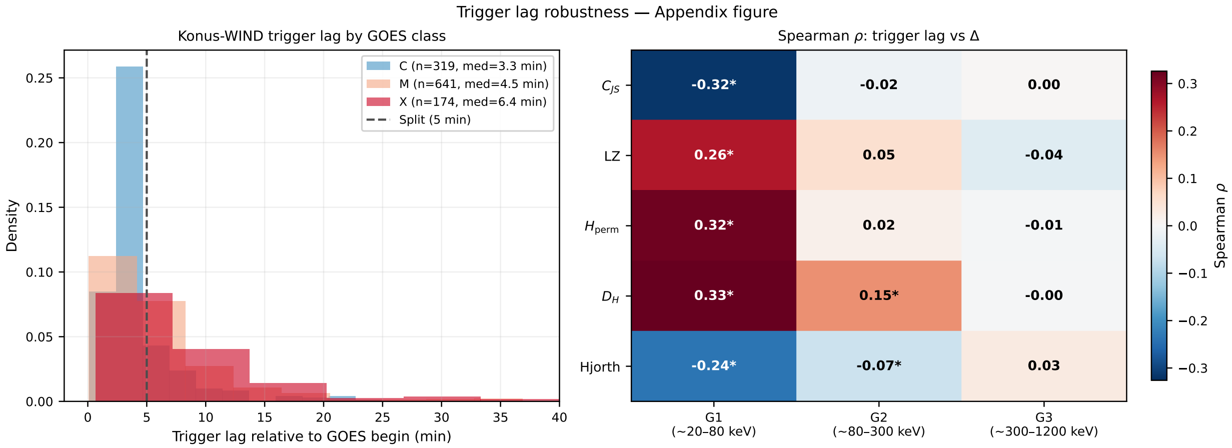

Figure 7: Trigger lag robustness analysis. *Left*: distribution of the temporal offset between the Konus-WIND trigger time and the GOES soft X-ray begin time, shown separately for C- (blue), M- (orange), and X-class (red) flares. The dashed vertical line marks the 300 s threshold used to define fast- and slow-trigger groups. The systematic increase of lag with flare class (medians: C 201 s, M 267 s, X 378 s) reflects the longer thermal precursor phase in more energetic events. *Right*: Spearman rank correlation (ρ) between trigger lag and Δ for each channel–descriptor combination. Values in G2 and G3 are universally small ($|\rho| < 0.15$); moderate correlations in G1 ($|\rho| \approx 0.24$–0.33) reflect the collinearity between lag and GOES class rather than a direct confounding effect.